Influence of TiO2 on the Microstructure, Mechanical Properties and Corrosion Resistance of Hydroxyapatite HaP + TiO2 Nanocomposites Deposited Using Spray Pyrolysis

Hafedh Dhiflaoui, Sarra Ben Salem, Mohamed Salah, Youssef Dabaki, Slah Chayoukhi, Bilel Gassoumi, Anouar Hajjaji, Ahmed Ben Cheikh Larbi, Mosbah Amlouk, Hicham Benhayoune

coatings

MDPI

Article

Influence of TiO_2 on the Microstructure, Mechanical Properties and Corrosion Resistance of Hydroxyapatite HaP + TiO_2 Nanocomposites Deposited Using Spray Pyrolysis

Hafedh Dhiflaoui [1,2,*], Sarra Ben Salem [1], Mohamed Salah [1], Youssef Dabaki [1,3], Slah Chayoukhi [4], Bilel Gassoumi [5], Anouar Hajjaji [6], Ahmed Ben Cheikh Larbi [1], Mosbah Amlouk [7] and Hicham Benhayoune [8,*]

1 Laboratoire de Mécanique, Matériaux et Procédés LR99ES05, Ecole Nationale Supérieure d'Ingénieurs de Tunis, Université de Tunis, Tunis 1008, Tunisia; sarrabensalem475@gmail.com (S.B.S.); bohr2011@gmail.com (M.S.); dabakiyoussef@gmail.com (Y.D.); ahmed.cheikhlarbi@gmail.com (A.B.C.L.)
2 Institut Supérieur des Sciences Appliquées et de Technologie de Kasserine, Université de Kairouan, Tunis 3100, Tunisia
3 Laboratoire de Physico-Chimie de l'Atmosphere, Université du Littoral Cote d'Opale, 59140 Dunkerque, France
4 Laboratoire Mécanique, Productique et Énergétique (LMPE), Ecole Nationale Supérieure d'Ingénieurs de Tunis, Université de Tunis, B.P. 56, Bab Menara, Tunis 1008, Tunisia; slah.chayoukhi@fst.utm.tn
5 Laboratoire Nanomatériaux, Nanotechnologie et Énergie (L2NE), Faculté des Sciences de Tunis, Université de Tunis El Manar, Tunis 2092, Tunisia; gassoumi.bilel@gmail.com
6 Laboratoire de Photovoltaïque, Centre de Recherches et des Technologies de l'Energie, Technopole de Borj-Cédria, BP 95, Hammam-Lif 2050, Tunisia
7 Department de Physique, Unité de Physique des Dispositifs à Semi-Conducteurs, Faculté des Sciences de Tunis, Tunis El Manar University, Tunis 2092, Tunisia; mosbah.amlouk@gmail.com
8 Institut de Thermique, Mécanique et Matériaux (ITheMM), Université de Reims Champagne-Ardenne (URCA), 51100 Reims, France
* Correspondence: dhafedh@gmail.com (H.D.); hicham.benhayoune@univ-reims.fr (H.B.)

Abstract: Titanium oxides and their alloys are widely used in medical applications because of their biocompatibility. However, they are characterized by their low resistance to corrosion. The HaP + TiO_2 nanocomposites' coating was applied in different experiments, especially on a Ti-6Al-4V substrate with the spray pyrolysis process to deal with such weakness. The TiO_2 content effects on the surface morphology and the phase composition were investigated using a scanning electron microscopy, X-ray microanalysis (SEM-EDXS) and X-ray diffraction (XRD). The mechanical properties were determined with nanoindentation. The potentiodynamic polarization, electrochemical impedance spectroscopy (EIS) and simulated body fluid (SBF) solution environment tests were carried out to investigate the corrosion resistance of HaP + TiO_2/Ti6Al4V systems. The experimental findings revealed that sprayed thin films possessed uniform morphology. The coatings' nanoindentations proved that the HaP + 20% TiO_2 coating hardness (252.77 MPa) and the elastic modulus (52.48 GPa) overtopped those of the pure hydroxyapatite coatings. The corrosion test demonstrated that the corrosion current density of about 36.1 μA cm^{-2} and the corrosion potential of the order of −392.7 mV of HaP + 20% TiO_2 was lower compared to the pure HaP coating.

Keywords: HaP nanocomposite; corrosion; nanoindentation; mocrosctructure

check for updates

Citation: Dhiflaoui, H.; Ben Salem, S.; Salah, M.; Dabaki, Y.; Chayoukhi, S.; Gassoumi, B.; Hajjaji, A.; Ben Cheikh Larbi, A.; Amlouk, M.; Benhayoune, H. Influence of TiO_2 on the Microstructure, Mechanical Properties and Corrosion Resistance of Hydroxyapatite HaP + TiO_2 Nanocomposites Deposited Using Spray Pyrolysis. *Coatings* **2023**, *13*, 1283. https://doi.org/10.3390/coatings13071283

Academic Editor: Maria Vittoria Diamanti

Received: 29 May 2023
Revised: 12 July 2023
Accepted: 19 July 2023
Published: 21 July 2023

1. Introduction

During the past decades, metallic implants (e.g., stainless steel, titanium, alloys, etc.) have been intensively used in different medical applications. The Ti-6Al-4Valloy is generally used as an implant in artificial hip and knee joints due to its low elastic modulus and its good biocompatibility [1,2]. However, the use of Ti-6Al-4V implants and their application in the human body can cause health problems due to the release of toxic aluminum (Al) and vanadium (V) ions that can damage the cells and tissues, and it may even lead to

cancer [3–5]. To overcome this deficit, surface modification consists of one of the envisaged solutions to reduce the release of Al and V ions and to improve their corrosive effect on human body fluids. Hydroxyapatite ($Ca_{10}(PO_4)_6(OH)_2$) has also attracted great interest in the medical field due to its excellent bioactivity and biocompatibility. Indeed, this material has become particularly interesting in artificial implants and human tissue restorations since it offers bone growth around the implant [6,7]. Moreover, its morphology an dits structure are similar to those of human hard tissues, especially those of bones and teeth. HaP-based bioactive coatings are the biomaterials that replace tissues in the body. They consist of nanoparticles similar to those of the inorganic molecules of human bones.

However, HaP coatings are generally synthesized using several methods such as physical vapor deposition (PVD) [8], sol–gel [9], micro-arc oxidation [10], plasma spray [11], etc. Among these techniques, spray pyrolysis shows some advantages, including uniformity in the coating's thickness, a high deposition rate, low cost and the ability to coat complex shapes and geometries. In addition, this technique can be used to produce crystalline coatings without applying post-heating [12]. HaP has unfavorable mechanical properties, which makes it unsuitable for load-bearing conditions. As it is brittle and weak, HaP's clinical application in orthopedics and dentistry is remarkably reduced [13]. Thus, several solutions were proposed to improve the long-term performance of this compound. For instance, the use of titanium and its alloys as bearing implants can be mentioned due to their excellent mechanical toughness, strength, biocompatibility and corrosion resistance [14,15]. The mechanical properties of HaP can be enhanced by employing other ceramic materials. This approach presents an alternative to improve the overall durability and strength of HaP in various applications. According to Lee et al. [16], ZrO_2, Al_2O_3 and their composite ceramics exhibit strong biocompatibility, exceptional oxidation resistance and high wear resistance, making them efficiently employed in both matrix and reinforcement phases. Tanaka et al. [17] used ZrO_2, La_2O_3 and TiO_2 as binding agents to improve HaP's bending and tensile strength. Also, Oktar [18] observed that the microstructure and phases formed during the sintering of the composite materials significantly influenced the densification and mechanical properties of the resulting composites. These composites, containing 5 wt% or 10 wt% of TiO_2, were made of HaP obtained from bovine bone. Recently, Vemulapalli et al. [19] have found that the mechanical properties (hardness, Young's modulus, fracture toughness, bending strength and compressive strength) of the composites (HaP/TiO_2), produced using ball milling, improved significantly with the addition of TiO_2 content. On the other hand, Ahmadi et al. [6] showed that TiO_2/HaP + 15 wt% of TiO_2 + 5 wt% of Ag coating had a higher adhesion strength (20.5 MPa), hardness (5.2 GPa) and elastic modulus (110.6 GPa), compared to the pure hydroxyapatite coatings. Indeed, they also showed that these coatings had the lowest corrosion current density (0.22 $\mu A/cm^2$).

To date, there are a few studies that have investigated the characterization of HaP + TiO_2 thin films with various TiO_2 contents in the literature, but they did not combine the study of microstructural properties with that of the nanomechanical and electrochemical characteristics [20,21]. The objective of this investigation is to grow HaP coatings on Ti-6Al-4V substrates, which have a structure most similar to that of human bone. Therefore, a detailed analysis of the mechanical and corrosion resistance of the deposited HaP + TiO_2 thin film seems to be in demand for the assessment of its reliability. The present contribution is in the detailed study of the correlation between the nanomechanical properties, corrosion performance in a simulated body fluid (SBF) medium, coating morphology and TiO_2 content.

2. Materials and Methods

2.1. Sample Preparations

Firstly, HaP + TiO_2 nanocomposites were successfully synthesized using an aqueous solution of 0.042 M of $Ca(NO_3)_2{\cdot}4H_2O$by adding 25 mL of a 5 mM acetic acid as a catalyst. TiO_2 nano-powder (particle size lower than 21 nm) [22], provided by Sigma-Aldrich, was added as a doping agent with varying amounts of 0%, 5%, 10% and 20% (calculated to total

weight of TiO_2). Then, the solution was stirred for 15 min. Cylindrical rods of Ti-6Al-4V of dimensions 12 mm × 4 mm were used as substrates. To accomplish the synthesis of the coatings, the substrates underwent both mechanical polishing with abrasive paper and chemical etching in diluted solution acids consisting of nitric acid (HNO_3, 6% in volume) and hydrofluoric acid (HF, 3% in volume) at room temperature for 30 s. Afterward, the substrates were ultrasonically cleaned with acetone for 15 min and washed with distilled water after each step.

Secondly, the substrates were gradually heated on a heating plate to prevent thermal shock. Once the desired synthesis temperature of 450 °C was reached, the solution was pumped at a fixed rate of 4 mL/min towards the sputtering device positioned at about 27 cm away from the substrates [23]. Nitrogen gas was employed as the carrier gas with a pressure of approximately 0.5 bars. Finally, the resulting coatings were cooled naturally for three hours until attaining room temperature (Figure 1) [24,25].

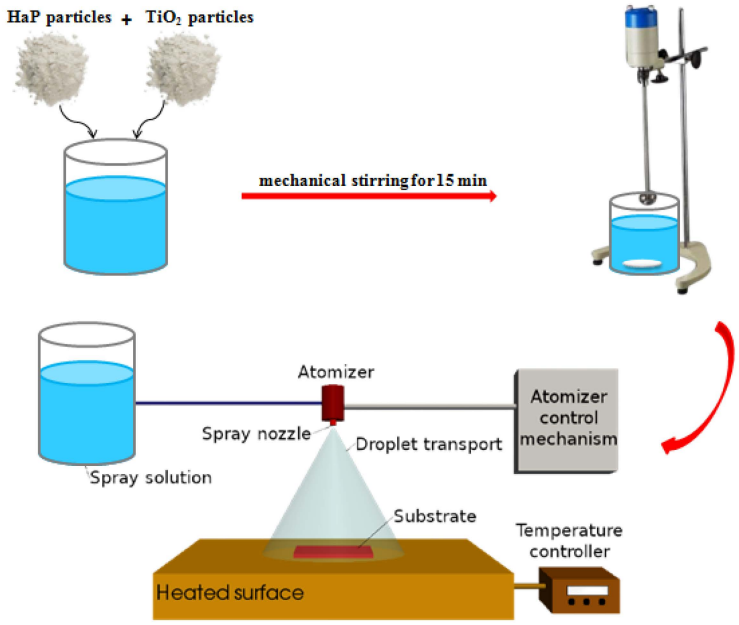

Figure 1. Sample preparations and principle of the spray pyrolysis process.

2.2. Characterization of the Coatings

The coatings morphology was characterized via a LaB6 electron microscope (Virginia Tech Switchboard, Blacksburg, CA, USA) operating at 0–30 kV. The chemical composition of the material was analyzed using both X-ray microanalysis (SEM-EDXS) (IXRF, Austin, TX, USA) and a scanning electron microscope (SEM) (IXRF, Austin, TX, USA). Furthermore, the phase identification and composition analysis were conducted with the help of a Bruker D8 Advance diffractometer (Bruker, Santa Barbara, CA, USA) utilizing X-ray diffraction techniques. The experiment involved adjusting the angle within a range of 2θ = 20 to 80° using monochromatic CuKα radiation. The increment between each measurement was set to 0.04°. The mechanical properties of the HaP + TiO_2 coatings were specified through nanoindentation. The nanoindentation tests were performed using an Anton Paar NHT^2 instrument in Anton Paar, Buchs, Switzerland). The equipment was fitted with a diamond Berkovich tip that featured a nominal angle of 65.3° and a nominal radius curvature of 20 nm. All samples were subjected to a consistent loading and unloading rate of 160 mN/min during the tests. The tests were restricted to a maximum load of 80 mN. During the tests, a nanoindentation technique was used with a Berkovich diamond tip that featured a nominal angle of 65.3° and a nominal radius with a curvature equal to 20 nm. The nanoindentation process was carried out using a nanoindenter instrument CSM type manufactured by Anton Paar, Buchs, Switzerland). The coatings' elastic modulus

(E_{IT}) and hardness (H_{IT}) were measured as part of the experiment. The measurements were reached by recording the indenter displacement as a function of the applied normal load. During the loading phase, the penetration depth increased until reaching a maximum value (P_{max}). After removing the indenter, the indentation depth declined to the residual indentation depth (h_r). Additionally, the hardness and elasticity modulus were determined by analyzing the discharge curve and applying the Oliver–Pharr model [26] that allowed their calculation, relying on the results presented by the discharge curve. As part of the analysis, the maximum load was divided by the projected area of the indenter in contact with the sample at the point of maximum load. This measurement was used as a factor in determining the hardness of the sample. Figure 2 depicts the typical curve of a nanoindentation test.

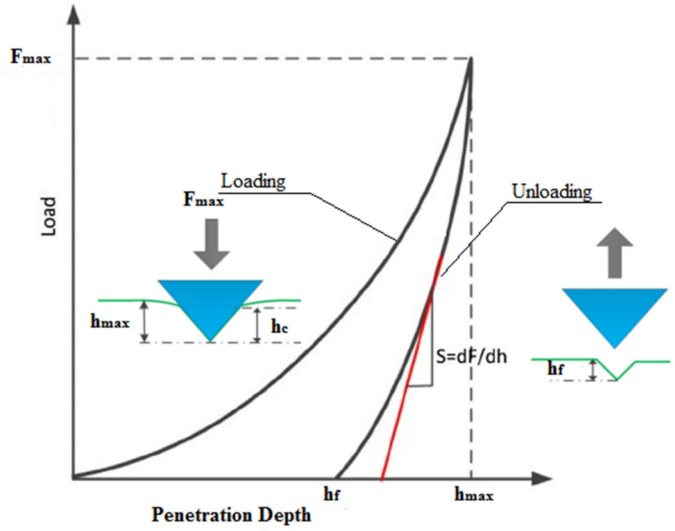

Figure 2. Typical curve of a nano-indentation test.

To assess how TiO_2 impacted the hardness and elastic modulus of HaP coatings, nanoindentation measurements were carried out in control mode. The maximum load in all the experiments was maintained at 80 mN. The loading and unloading rates were set to 160 mN/min. To ensure that the test results were reliable and accurate, each test was conducted five times.

Electrochemical measurements were conducted using the Ec-Lab system (Biologic, Seyssinet-Pariset, France) (version V11.50) made up of a Potentiostat–Galvanostat PGZ301 at room temperature in a three-electrode cell: (i) a saturated calomel reference electrode (SCE) (Hg/Hg_2Cl_2) filled with 1 M KCl and employed to measure the potential; (ii) an auxiliary electrode consisting of a coiled nickel wire; and (iii) a working electrode (test sample). The Tafel graphs are measured in the potential range of [−200 mV; +200 mV] at 1 mV/s. The polarization curves of Ti-6Al-4V and Ti-6Al-4Vcoatingswere generated while in a simulated body fluid solution at a temperature of 37 °C. To ensure their reliability, each corrosion test was conducted three times. The main components of the used solution are listed in Table 1.

To examine the electrochemical behavior of the samples, electrochemical impedance spectra (EIS) measurements were carried out within a frequency span of 10 mHz to 10 kHz. The ZSimpWin software (Gamry Instruments, Warminster, PA, USA) (version 3.5) was used to model and interpret the results via an equivalent circuit. The following Figure 3 summarizes all the test instruments and product materials used in this work.

Table 1. Chemical composition of SBF solution [27].

Component	Amount in 1000 mL
NaCl	8.035 g
$NaHCO_3$	0.355 g
KCl	0.225 g
$MgCl_2.6H_2O$	0.311 g
Na_2SO_4	0.072 g
1.0 M HCl	39 mL
$CaCl_2$	0.292 g
$((HOCH_2)_3CNH_2)$	6.118 g

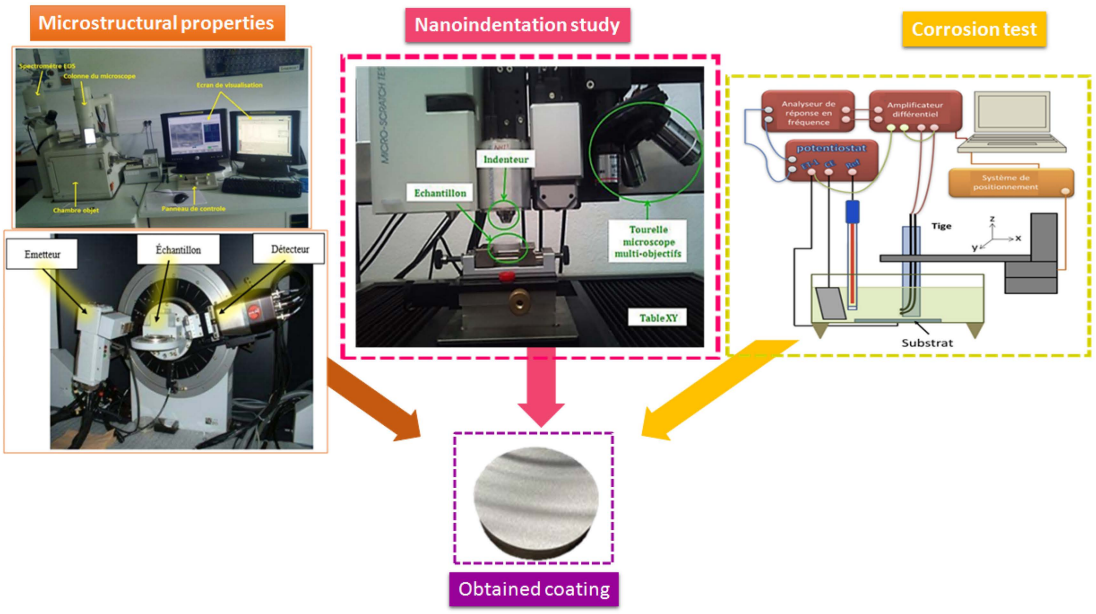

Figure 3. Macro photograph of the used test instruments.

3. Results and Discussion

3.1. Effect of TiO_2 Contents on the Morphologies and Microstructural Properties

The SEM images of HaP + TiO_2 coatings are presented in Figure 4. The experimental results show that the sprayed coatings possessed a homogeneous surface without any cracks or holes. Moreover, the TiO_2 particles were evenly distributed throughout the film. It was also noticed that the shape and uniformity of the grains were affected by the concentration of doping in the TiO_2 material. At a 20% doping concentration, the grains had a more uniform and spherical shape. However, a 10% concentration resulted in non-uniform and irregularly shaped grains. The results show that the addition of TiO_2 played a crucial role in determining the morphology and size of the HaP. For instance, Nathanael et al. [28] reported that the presence of the crystallized TiO_2 anatase phase promoted the molecular ordering of Ca and P ions, which ordinarily occurred in a random distribution resulting in the formation of the apatite structure. They also showed that the anatase phase of TiO_2 stimulated the nucleation and growth of HaP more than the rutile phase due to the better lattice compatibility between anatase TiO_2 and HaP.

EDX proved that, when the content of TiO_2 increased, the obtained Ca/P ratio for the HaP-coated sample was 1.74 and reduced to the range of HaP + 5% TiO_2 (1.73), HaP + 10% TiO_2 (1.71) and HaP + 20% TiO_2 (1.68) when the TiO_2 content increased. The Ca/P ratios between 1.67 and 1.76 are suitable as standard ratios for bioimplant coatings [29].

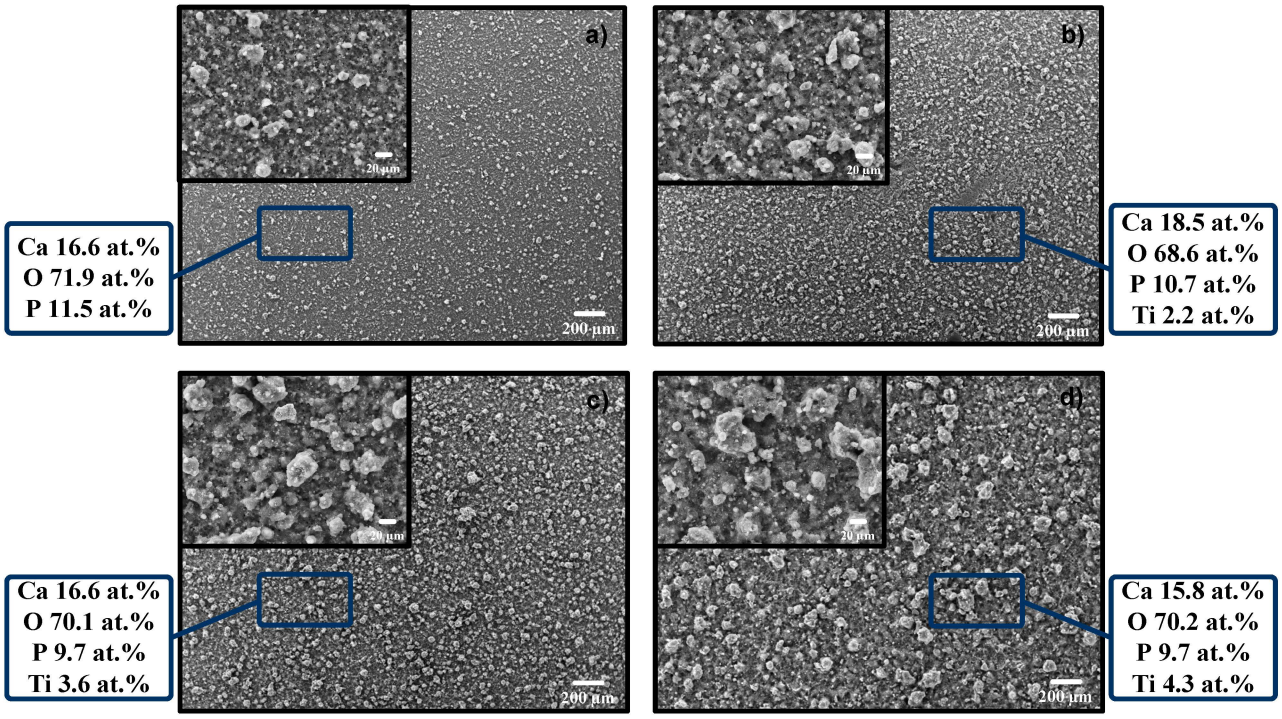

Figure 4. SEM images of HaP and HA/TiO_2 coatings. (**a**) HaP, (**b**) HaP + 5% TiO_2, (**c**) HaP + 10% TiO_2 and (**d**) HaP + 20% TiO_2.

The XRD patterns for the samples HaP, HaP + 5% TiO_2, HaP + 10% TiO_2 and HaP + 20% TiO_2 are presented in Figure 5. According to the XRD patterns, the HaP peaks were observed in positions 2θ = 31°, 78°, 51°, 52°, 69° and 74°. The diffraction peaks observed were consistent with the pure hexagonal phase, which arein agreement with the bulk hydroxyapatite crystals and can be easily indexed (JCPDS#9-432). The addition of TiO_2 resulted in the appearance of the phase in positions 2θ = 26.1°, 36.8°, 47.55°, 54.1°, 55.61°, 66.3° and 73.4° (JCPDS#84-1286) [30,31]. All X-ray peaks could be indexed along with the Tetragonal phase.

We noticed that the diffraction pattern was almost identical to that of pure HaP, although with a slight decrease in the intensity of HaP peaks. Also, in nanocomposites containing 20% of TiO_2, the TiO_2 phase was dominated. The introduction of TiO_2 in the early stages initiated the nucleation of nanorods and accelerated their growth through a process of heterogeneous nucleation [32,33]. Nathaniel et al. [34] showed that after the addition of 40% TiO_2, the excess of $Ti(OH)_4$washydrolyzed, nucleated as spherical particles and deposited on the surface of the HaP nanorods. They found that the lattice parameters for the HaP phase varied, with parameters (a) and (c) decreasing from 9.418 to 9.397 Å and from 6.884 to 6.801 Å, respectively. Likewise, for the TiO_2 phase, parameters "a" and "c" increased, respectively, from 3.785 to 3.823 Å and from 9.513 to 9.585 Å. These variations were assigned to the presence of TiO_2 in the HaP structure. Hence, as more TiO_2 was added and covered the HaP phase's surface, the intensity of the XRD peak of HaP was decreasing [28]. Observations indicated that as the concentration of TiO_2 increased, there was a broadening in the XRD peaks, and this resulted in a decrease in the crystallite size decrease. The crystallite size of the composites was estimated from Scherrer's formula (Equation (1)) [35,36]:

$$D = 0.9\lambda/B{\cdot}\cos\theta \quad (1)$$

where λ is the X-ray wavelength, θ represents the diffraction angle and B corresponds to the full width at the diffraction peak half maximum.

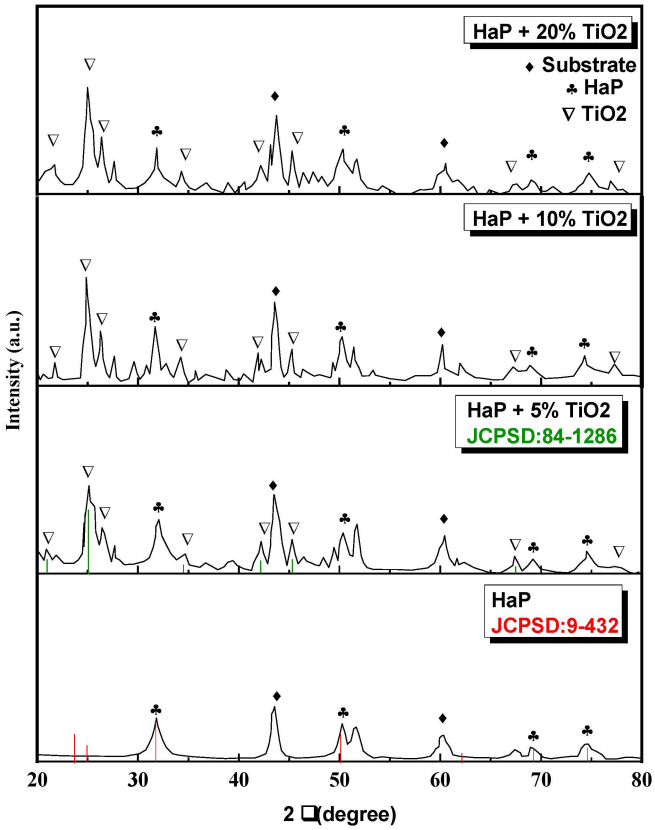

Figure 5. X-ray diffraction pattern of HaP and HaP/TiO_2 composites.

The result shows a gradual decrease in the crystallite size from 52 nm (5% TiO_2) to 20 nm with a 20% increase inTiO_2 amount.

3.2. Effect of TiO_2Contents on the Hardness and the Elastic Modulus

The evolution of the applied load according to the penetration depth provided by the nanoindentation for different coatings is depicted in Figure 6. The experimental findings exhibit a similar trend in which the maximum displacement declined due to the addition of TiO_2. The numerical data of the hardness (H) and the elastic modulus (E) are gathered in Table 2.

Table 2 and Figure 6 demonstrate that the pure HaP coating exhibited the lowest hardness (98.98 MPa) and elastic modulus (21.29 GPa), compared to the other coatings. By adding 5% of TiO_2, the hardness and elastic modulus rose to 122.86 MPa and 30.13 GPa, respectively. Many researchers proved that the addition of TiO_2 to HaP leads to a decrease in the grain size of the used material, as observed in the increase of both the hardness and the elastic modulus. This increase was attributed to the relationship between the nano-hardness, elastic modulus, grain size and crystal size. This relation shows that the decrease in the grain size led to an improvement in the latter properties [4,7,17]. The highest hardness and Young's modulus values of 252.77 MPa and 52.48 GPa were obtained from the20% TiO_2 nanocomposite. From the experimental results, it was found that the addition of TiO_2 remarkably enhanced the Young's modulus and the hardness of the HaP/TiO_2 composites. Refs. [28,37] show that the microstructural and morphological modifications due to the addition of TiO_2 on HaP have a strong influence on the mechanical properties of the composite coating. According to the results regarding the nanoindentation test, it was noted that a progressive increase in the mechanical properties of hardness and Young's modulus was found as the content of TiO_2 reinforcement increased. Also, the test depicted that the HaP + 20% TiO_2 coating had the highest hardness value, while the pure HaP-coated sample had the lowest hardness.

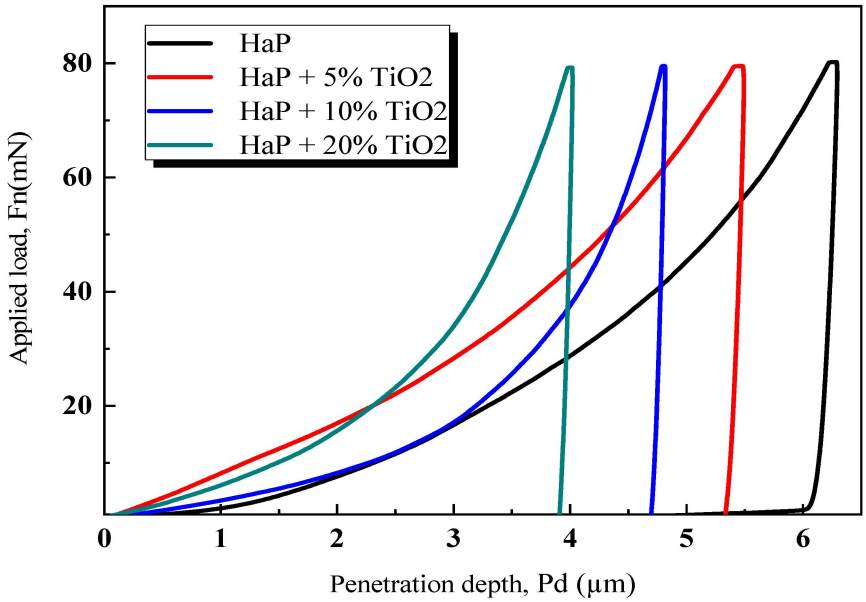

Figure 6. Force–penetration depth curves for HaP, HaP + 5% TiO_2, HaP + 10% TiO_2 and HaP + 20% TiO_2 coatings.

Table 2. Nanoindentation results of the different used coatings.

Sample	H (MPa)	E (GPa)
HaP	98.98 ± 1.81	21.29 ± 0.13
HaP + 5% TiO_2	122.86 ± 2.2	30.13 ± 0.22
HaP + 10% TiO_2	172.18 ± 1.52	42.74 ± 0.34
HaP + 20% TiO_2	252.77 ± 1.63	52.48 ± 0.51

3.3. Effect of TiO_2 Contents on the Corrosion Properties of the Coatings

The Tafel extrapolation technique, demonstrated in the polarization curves, was utilized to provide several corrosion parameters (e.g., Tafel constants (β_a and β_c), corrosion potential (E_{corr}) and corrosion current density (I_{corr})). Afterward, the polarization resistance (R_p) was computed using the typical Stern–Geary equation [21]. Figure 7 presents the Tafel curves given by the polarization tests, while Table 3 shows the obtained values.

$$R_p = \frac{\beta_a \times \beta_c}{2.303(\beta_a + \beta_c) i_{corr}} \quad (2)$$

The obtained results reveal that the coated samples had a superior E_{corr} compared to the uncoated substrate. The corrosion current density I_{corr} of the uncoated substrate was equal to 38.80 × 10^{-2} (mA cm^{-2}), indicating poor corrosion resistance. Although the introduction of HaP coatings remarkably minimized the corrosion current density to 267 µA cm^{-2}, the appearance ofcracks in the pure HaP coating made it possible to expose the surface of the substrate to the SBF solution under such high current density.

A similar result was obtained by Fathi et al. [38] for HaP coatings on implant materials in simulated body fluids. The authors showed that the corrosion potential E_{corr} value of the coated sample (358.79 mV) shifted to a valuable amount, compared to that of the substrate (−363.96 mV). This result further confirmed that the coated samples had superior passivation than the substrate. Amaravathy et al. [39] found that, in comparison to the uncoated sample, the HaP-coated substrate exhibited a higher corrosion potential and less corrosion current density. As it was observed that the pure HaP coatings had less adhesion behavior, resulting in these coatings breaking easily and losing barrier properties. Such behavior allowed the simulatedbody fluid (SBF) to penetrate the cracks and pores. Byanalyzing the results, it was concluded that the HaP + TiO_2 coatings could provide

better corrosion protection than the pure HaP coatings. Moreover, with the rise of TiO_2 in HaP, the I_{corr} value declined, and the HaP + 20% TiO_2-coated sample showed the lowest I_{corr} value. Moskalewicz et al. [40] demonstrated that adding TiO_2 coatings resulted in the corrosion resistance increase of the metallic substrate. This finding was observed because of their homogeneous microstructure and very good adhesion to the substrate. In fact, the corrosion potential rose from ~−0.62 (potential of the cathodicanodic transition of the pristine Co-28Cr-5Mo alloy) to about −0.48 V for the HaP and to−0.59 V for the TiO_2/HaP coatings.

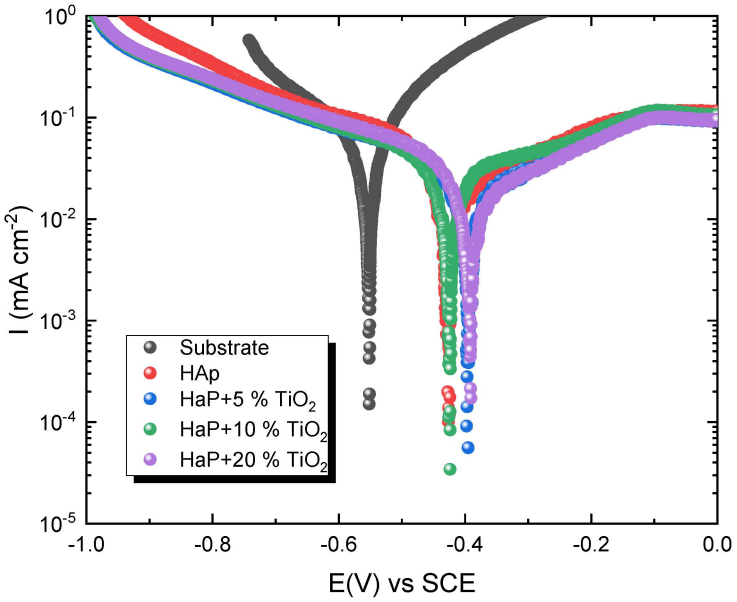

Figure 7. Tafel polarization curves of the uncoated and coated samples.

Table 3. Corrosion parameter values obtained from Tafel curves.

Coating	E_{corr} (mV)	I_{corr} (μA cm^{-2})	β_a	β_c	R_p (kΩ cm^2)
Substrate	−553.3 ± 1.33	204 ± 0.81	0.10	01.80	0.89
HaP	−427.5 ± 1.21	38.9 ± 0.17	0.10	20.31	1.19
HaP + 5% TiO_2	−424.9 ± 1.27	388.0 ± 0.88	0.10	01.33	0.10
HaP + 10% TiO_2	−392.8 ± 1.36	267 ± 0.93	0.10	02.80	0.15
HaP + 20% TiO_2	−392.7 ± 1.53	36.1 ± 0.13	0.10	15.57	1.10

The results obtained in this study reveal that the corrosion resistance of the HaP coating in SBF solution is significantly increased with TiO_2 content. The sample coated with HaP + 20% TiO_2 revealed a lower corrosion current of 36.1 μA cm^{-2} and a corrosion rate of 1.1 c kΩ cm^2, compared to the uncoated Ti-Al6-4V sample.

3.4. Electrochemical Impedance Spectroscopy (EIS)

The electrochemical impedance spectroscopy (EIS) is widely known as an effective technique applied to study the corrosion behavior of the used materials in the interface between the coatings and the electrolytes. Based on EIS, the corrosion resistance property of the elaborated coatings (e.g., the behavior of the dual-layer capacitance and charge transfer resistance) was determined. In Figure 8, the Nyquist plots of the impedance diagrams of both the Ti-6Al-4V substrate and the HaP + TiO_2 coatings are presented. To simulate the experimental data, the EIS results were fitted through an equivalent circuit using the ZSimpWin software. As shown in Figure 9, the equivalent circuit model consists of the following elements: R_s (solution resistance), R_p (coating resistance), R_{ct} (charge transfer resistance at the electrode–electrolyte interface), Q_{dl} (double-layer capacitance)

and Q_c (interfacial capacitance). The different value parameters fitting the circuit model are detailed in Table 4.

Table 4. The fitting parameters of the equivalent circuit.

Coating	R_s (Ω cm^2)	CPE_c		R_p (Ω cm^2)	CPE_{dl}		R_{ct} (Ω cm^2)	$\chi^2 \times 10^{-4}$
		Y_c (mF cm^{-2})	n_c		Y_{dl} (mF cm^{-2})	n_{dl}		
Substrate	13.88	02.67	0.58	056.21	76.8	1.00	01.53	1.47
HaP	09.48	11.86	0.45	075.17	78.1	0.86	11.22	9.5
HaP + 5% TiO_2	16.71	17.59	0.38	142.90	157	0.88	41.85	1.85
HaP + 10% TiO_2	07.68	55.20	0.71	208.70	19.7	0.38	97.94	3.03
HaP + 20% TiO_2	17.36	18.06	0.70	214.00	10.9	0.40	697.10	2.36

During the modeling calculation, an iterative approach is adopted herein using the chi-square (χ^2) value for the model along with the percentage error values for each circuit component. This was conducted to ascertain the effectiveness of a particular model in fitting the experimental data. The calculation of the (χ^2) value was based on the expression mentioned below.

$$\chi^2 = \sum_{i=1}^{i=n} [W_i'(Z'_{i,exp} - Z'_{i,cal}(\omega_i, \overline{p})^2 + W_i'' (Z''_{i,exp} - Z''_{i,cal}(\omega_i, \overline{p}))^2] \quad (3)$$

The experimental (calculated) impedance at a particular frequency is represented by its real and imaginary parts, denoted by $Z'_{i,exp}$ ($Z'_{i,cal}$) and $Z''_{i,exp}$($Z''_{i,cal}$), respectively. The statistical weights of the data are denoted by these quantities as well. Also, the number of data points 'i' is represented by the variable 'n'.

Achieving the correlation between the experimental and theoretical data was determined by minimizing the value of the (χ^2). This was accomplished with the calculation of the difference between the experimental data and squaring it, which emphasized large variances in the data. The literature [41] reported that a value of one order of magnitude less than or equal to 10^{-3} is generally considered acceptable for a given model.

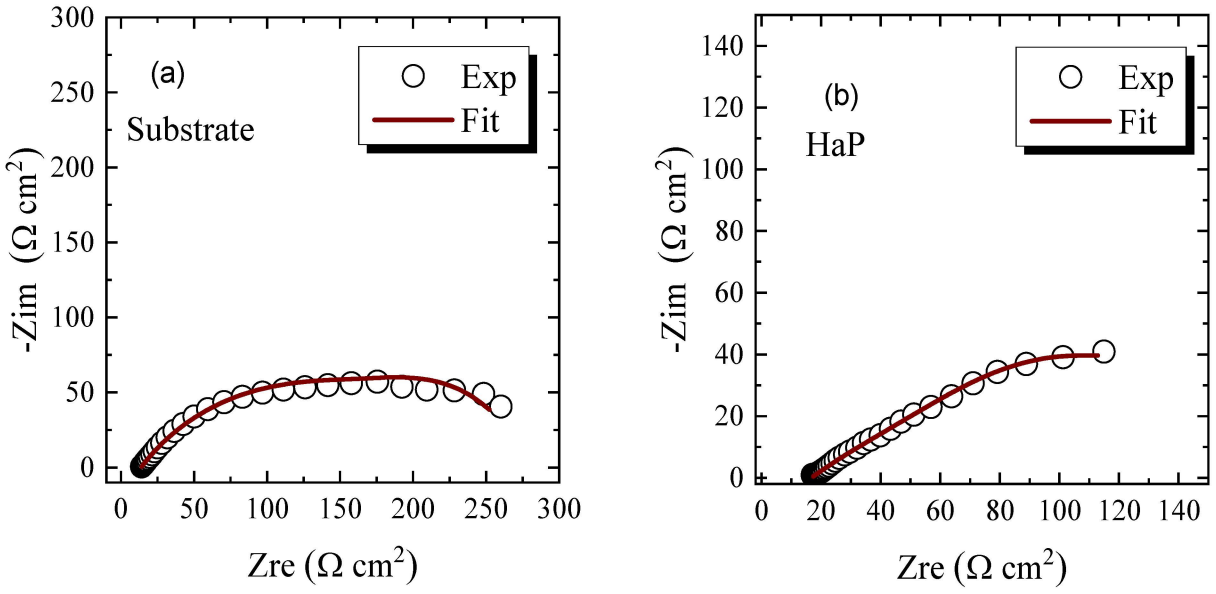

Figure 8. *Cont.*

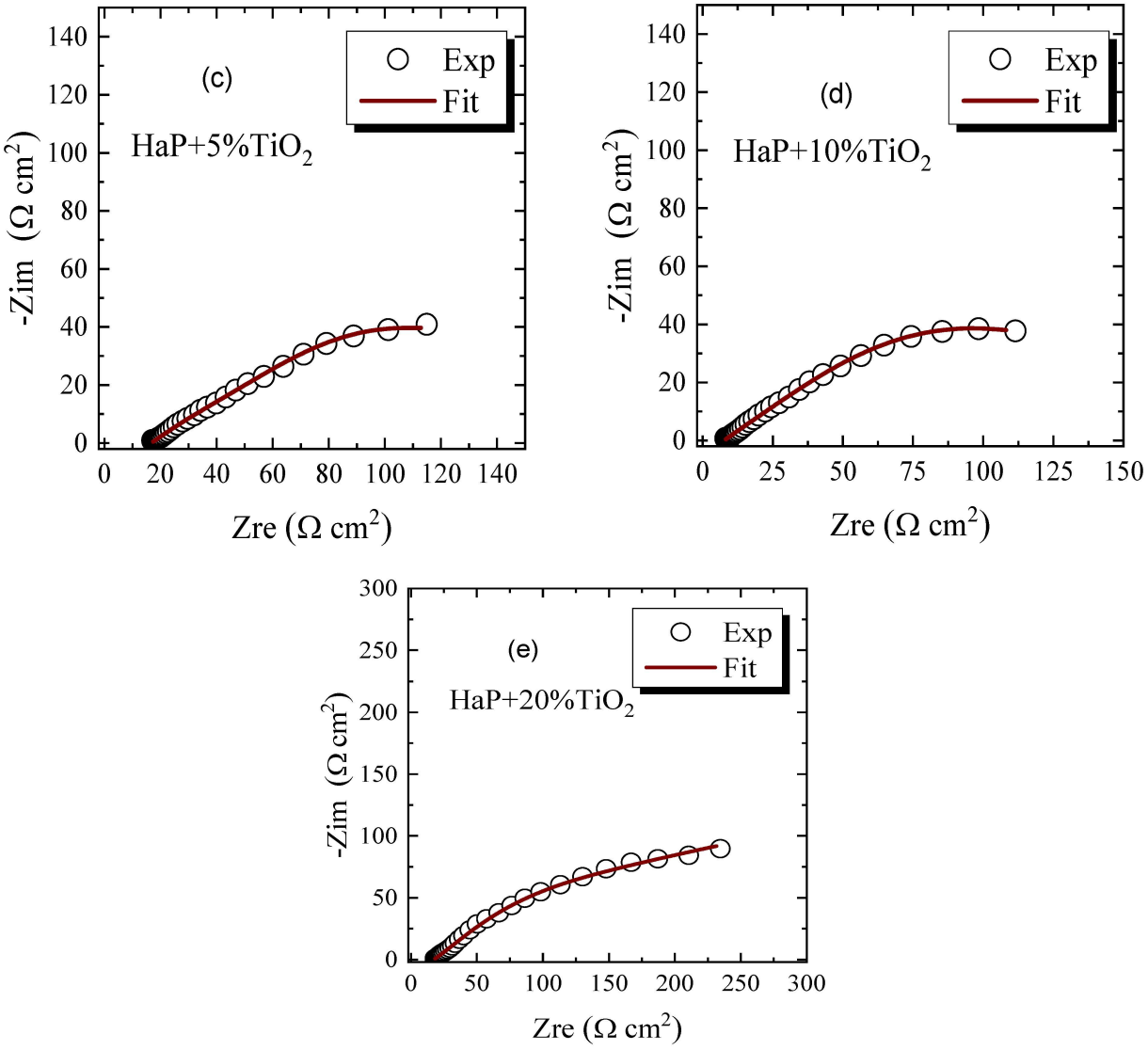

Figure 8. Nyquist experimental and modeling curves. (**a**) Substrate, (**b**) HaP, (**c**) HaP + 5% TiO_2, (**d**) HaP + 10% $TiO_2$and, (**e**) HaP + 20% TiO_2.

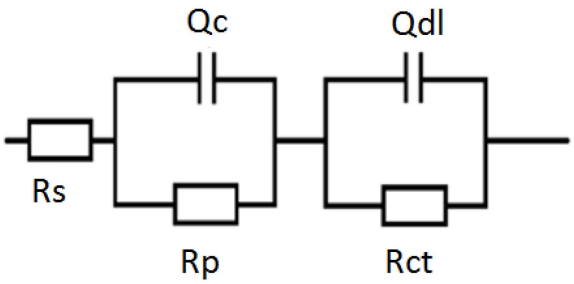

Figure 9. Equivalent circuits.

As revealed in the latter, the increase in TiO_2 content corresponds to the rise inthe charge transfer resistance R_{ct} (or corrosion resistance) of the HaP coatings. The values of R_{ct} range from 55.51 to 697.10 Ω cm^2. These findings are consistent with the results obtained by analyzing the Tafel curves. R_p increased from 56.21 to 214.00 Ω cm^2, suggesting the better corrosion resistance of HaP + TiO_2 coatings compared to that of the uncoated substrate. The observed behavior provided evidence that the enhanced corrosion resistance

of the sprayed coatings was attributed to the formation of a stable structure and a uniformly smooth surface that effectively prevented the penetration of the electrolytes.

As per Ahmadi et al. [6,42], the formation of a HaP layer causes a substantial increase in the diameter of the resistance semicircle (5.3×10^4 Ω cm^2). The polarization outcomes confirmed that an interface layer of TiO_2 leads to a reduction in the corrosion current density. The semicircle diameter for coatings that contained a TiO_2 interlayer was larger than that of the substrate or the pure HaP coating. It was also observed that the sample TiO_2/HaP + 15 wt% of TiO_2 + 5 wt% of Ag exhibited the largest semicircle diameter (6.54×10^5 Ω cm^2), indicating that it offers the highest resistance to corrosion.

To study in detail the interface between the electrolyte and the coated material, it is important to examine the double-layer capacitance (C_{dl}) calculated using the expression writtenbelow:

$$C_{dl} = \frac{(Y_{dl} \cdot \times R_{ct})^{\frac{1}{n_{dl}}}}{R_{ct}} \quad (4)$$

where Y_{dl} and n_{dl} are, respectively, the admittance and the exponent parameters.

In order to determine the surface roughness factor (f), the following expression was used:

$$f = \frac{C_{dl}}{22 \mu F cm^{-2}} \quad (5)$$

The customary value of the capacitance (C_{dl}) for metal electrodes was almost equal to 20 μF cm^{-2} [43].

For the real surface area, S_r, the following expression was utilized:

$$S_r = S \times f \quad (6)$$

where S is the geometric surface area of the coatings (~1 cm^2).

The formula applied to calculate the coating capacitance (C_c) is written below:

$$C_c = \frac{(Y_c \cdot R_c)^{\frac{1}{n_c}}}{R_c} \quad (7)$$

The values of C_{dl}, C_c and S_r are presented in Table 5.

Table 5. The double-layer capacitance (C_{dl}), the film capacitance (C_c) and the real surface area S_r of HaP + TiO_2 coatings.

Coating	C_{dl} (mF cm^{-2})	S_r(cm^2)	C_c (mF cm^{-2})
Substrate	0.076	3.8	0.017
HaP	0.076	2.2	0.37
HaP + 5% TiO_2	0.20	9.1	0.79
HaP + 10% TiO_2	0.057	2.3	0.98
HaP + 20% TiO_2	0.22	10.3	0.18

The results shown in Figure 10 reveal that the double-layer capacitance (C_{dl}) initially decreases. Then, it increases with the rise in the TiO_2 concentration. This observation suggests that the thickness of the corrosive layer formed on the HaP surface was reduced due to changes on the surface which, in turn, enhanced the anti-corrosive properties of the HaP + TiO_2 coatings.

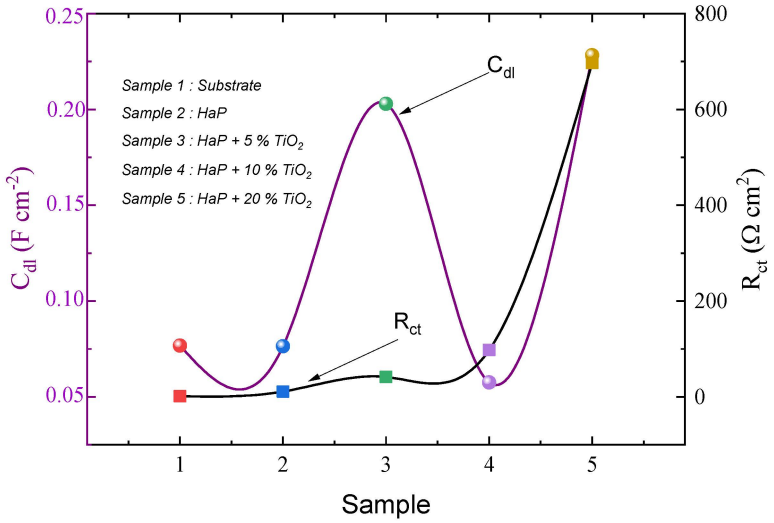

Figure 10. Variation of the charge transfer resistance (*Rct*) and the double-layer capacitance (*Cdl*) with different TiO_2 contents.

As displayed in Figure 11, the real surface area is larger than the geometric surface. Indeed, it increases with the rise in the TiO_2 concentration. This observation can be attributed to the surface roughness and heterogeneity rather than to its homogeneity.

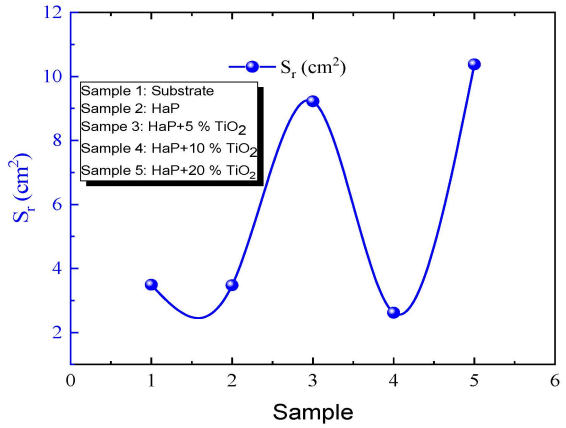

Figure 11. The real surface area, S_r.

The Bode diagrams of impedance and the phase for different coatings in the SBF solution are presented in Figure 12. The Bode plot generally shows that higher values of |Z| at lower frequencies indicate higher levels of corrosion resistance. Based on the result presented in Figure 12a, it can be inferred that the HaP + 20% TiO_2 coating has the highest corrosion resistance due to its higher Z modulus at low frequencies. The lowest Z modulus is related to the uncoated substrate. The electrochemical response of the HaP + 20% TiO_2 coating, as shown by the slope in the data, suggests that its electric double-layer capacitance is mostly capacitive. This observation implies that the coating has the potential to effectively minimize the corrosion rate of Ti-6Al-4V when exposed to SBF [41]. According to the Bode plots of the phase exposed in Figure 12b, a capacitive behavior results from the maximum phase angle occurring at low frequencies. At high frequencies, the impedance is not affected by frequency, while the phase angle approaches 0°, indicating a resistive behavior that corresponds to the resistance of the SBF solution between the working and reference electrodes. Conversely, in the low-frequency region, the HaP + 20% TiO_2 coating demonstrates a phase angle approaching −35°. This value indicates the capacitive behavior of the electrode–electrolyte interface.

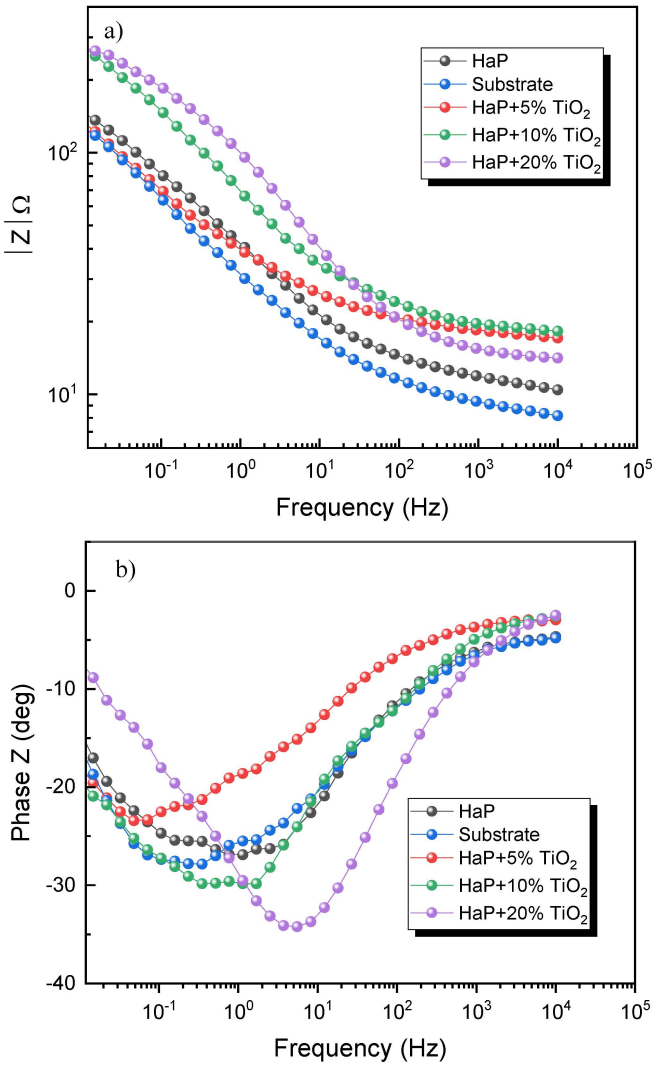

Figure 12. Bode impedance (**a**) and Bode phase diagram (**b**).

4. Conclusions

In summary, the spray technique was used to prepare nanocomposite thin films consisting of hydroxyapatite doped with titanium oxides. To determine the optimal structure of the thin oxide films, we conducted an X-ray diffraction analysis on the various deposits, examining the effect of the doping concentration. We also investigated some mechanical properties related to HaP in terms of TiO_2 content. These findings indicated that TiO_2 doping has a significant effect on the microstructural, morphological, and nanomechanical properties, as well as the corrosion rate, of HaP + TiO_2 coatings. The major obtained findings are presented below:

1. XRD results stand for the presence of HaP and TiO_2 compounds with no additional phases, while SEM micrographs revealed homogeneously distributed grain coatings;
2. The use of the nanoindentation test revealed that TiO_2 doping plays a crucial role in enhancing HaP thin films' mechanical properties, such as hardness and Young's modulus;
3. The corrosion studies using potentiodynamic polarization measurements as well as EIS techniques showed that TiO_2-doped HaP coatings exhibit much-improved corrosion resistance properties when compared to that of pure HaP thin films. This investigation is particularly noteworthy since we used a cost-effective, straightforward spray pyrolysis technique to obtain HaP thin films. Along the same line, these

TiO_2-doped films hold considerable potential for various applications, especially in environmental areas like photocatalysis, as well as in protective coating systems.

Author Contributions: Writing—original draft, H.D., S.B.S., M.S., Y.D., S.C., B.G. and H.B.; Supervision, A.H., A.B.C.L., M.A. and H.B. All authors have read and agreed to the published version of the manuscript.

Funding: This research received no external funding.

Institutional Review Board Statement: Not applicable.

Informed Consent Statement: Not applicable.

Data Availability Statement: Not applicable.

Conflicts of Interest: The authors declare no conflict of interest.

References

1. Ling, H.; Ling, P.; Wei, Z.; Zibo, N.; Xuan, C.; Maolin, C.; Qinzhao, Z.; Wenqian, P.; Peng, X.; Yang, L. Thermal corrosion behavior of $Yb_4Hf_3O_{12}$ ceramics exposed to calcium-ferrum-alumina-silicate (CFAS) at 1400 °C. *J. Eur. Ceram. Soc.* **2023**, *43*, 4114–4123.
2. Ling, P.; Ling, H.; Zibo, N.; Peng, X.; Wei, Z.; Yang, L. Corrosion behavior of ytterbium hafnate exposed to water-vapor with $Al(OH)_3$ impurities. *J. Eur. Ceram. Soc.* **2023**, *43*, 612–620.
3. Tlotleng, M.; Akinlabi, E.; Shukla, M.; Pityana, S. Microstructures, hardness and bioactivity of hydroxyapatite coatings deposited by direct laser melting process. *Mater. Sci. Eng. C* **2014**, *3*, 189–198. [CrossRef]
4. Nicholson, J.W. Titanium alloys for dental implants: A review. *Prosthesis* **2020**, *2*, 11. [CrossRef]
5. Okazaki, Y.; Gotoh, E. Implant applications of highly corrosion-resistant Ti-15Zr-4Nb-4Ta alloy. *Mater. Trans.* **2002**, *43*, 2943–2948. [CrossRef]
6. Ahmadi, R.; Asadpourchallou, N.; Kaleji, B.K. In vitro study: Evaluation of mechanical behavior, corrosion resistance, antibacterial properties and biocompatibility of $HAp/TiO_2/Ag$ coating on $Ti6Al4V/TiO_2$ substrate. *Surf. Interfaces* **2021**, *24*, 101072. [CrossRef]
7. Mohan, L.A.; Durgalakshmi, D.; Geetha, M.; Narayanan, T.S.; Asokamani, R. Electrophoretic deposition of nanocomposite (Hap + TiO_2) on titanium alloy for biomedical applications. *Ceram. Int.* **2012**, *38*, 3435–3443. [CrossRef]
8. Duta, L. In vivo assessment of synthetic and biological-derived calcium phosphate-based coatings fabricated by pulsed laser deposition: A review. *Coatings* **2021**, *11*, 99. [CrossRef]
9. Singh, N.; Batra, U.; Kumar, K.; Siddiquee, A.N. Evaluating the Electrochemical and In Vitro Degradation of an HA-Titania Nano-Channeled Coating for Effective Corrosion Resistance of Biodegradable Mg Alloy. *Coatings* **2023**, *13*, 30. [CrossRef]
10. Wang, Z.; Ye, F.; Chen, L.; Lv, W.; Zhang, Z.; Zang, Q.; Lu, S. Preparation and degradation characteristics of MAO/APS composite bio-coating in simulated body fluid. *Coatings* **2021**, *11*, 667. [CrossRef]
11. Heimann, R.B. Structural Changes of Hydroxylapatite during Plasma Spraying: Raman and NMR Spectroscopy Results. *Coatings* **2021**, *11*, 987. [CrossRef]
12. Farooq, S.A.; Raina, A.; Mohan, S.; Arvind Singh, R.; Jayalakshmi, S.; Irfan Ul Haq, M. Nanostructured coatings: Review on processing techniques, corrosion behaviour and tribological performance. *Nanomaterials* **2022**, *12*, 1323. [CrossRef]
13. Samanipour, F.; Bayati, M.R.; Zargar, H.R.; Golestani-Fard, F.; Troczynski, T.; Taheri, M. Electrophoretic enhanced micro arc oxidation of ZrO_2–HAp–TiO_2 nanostructured porous layers. *J. Alloys Compd.* **2011**, *509*, 9351–9355. [CrossRef]
14. Liu, X.; Chu, P.K.; Ding, C. Surface modification of titanium, titanium alloys, and related materials for biomedical applications. *Mater. Sci. Eng. R Rep.* **2004**, *47*, 49–121. [CrossRef]
15. Kunze, J.; Müller, L.; Macak, J.M.; Greil, P.; Schmuki, P.; Müller, F.A. Time-dependent growth of biomimetic apatite on anodic TiO_2 nanotubes. *Electrochim. Acta* **2008**, *53*, 6995–7003. [CrossRef]
16. Lee, B.T.; Jang, D.H.; Kang, I.C.; Lee, C.W. Relationship between Microstructures and Material Properties of Novel Fibrous Al_2O_3–(m-ZrO_2)/t-ZrO_2 Composites. *J. Am. Ceram. Soc.* **2005**, *88*, 2874–2878. [CrossRef]
17. Tanaka, A.; Nishimura, Y.; Sakaki, T.; Fujita, A.; Shin-Ike, T. Histologic evaluation of tissue response to sintered lanthanum-containing hydroxyapatites subcutaneously implanted in rats. *J. Osaka Dent. Univ.* **1989**, *23*, 111–120. [PubMed]
18. Oktar, F.N. Hydroxyapatite–TiO_2 composites. *Mater. Lett.* **2006**, *60*, 2207–2210. [CrossRef]
19. Vemulapalli, A.K.; Penmetsa, M.R.; Nallu, R.; Siriyala, R. HAp/TiO_2 nanocomposites: Influence of TiO_2 on microstructure and mechanical properties. *J. Compos. Mater.* **2020**, *54*, 765–772. [CrossRef]
20. Patrick, L.; Jonathan, A.; Stephen, M.; Jeroen, J.J.P.; Joanna, W.; Adrian, B.; Brian, J.M. Nanoindentation and nano-scratching of hydroxyapatite coatings for resorbable magnesium alloy bone implant applications. *J. Mech. Behav. Biomed. Mater.* **2022**, *133*, 105306.
21. Ivanova, A.A.; Surmeneva, M.A.; Tyurin, A.I.; Pirozhkova, T.S.; Shuvarin, I.A.; Prymak, O.; Epple, M.; Chaikina, M.V.; Surmenev, R.A. Fabrication and physico-mechanical properties of thin magnetron sputter deposited silver-containing hydroxyapatite films. *Appl. Surf. Sci.* **2016**, *360*, 929–935. [CrossRef]

22. Dhiflaoui, H.; Khlifi, K.; Barhoumi, N.; Ben Cheikh Larbi, A. The tribological and corrosion behavior of TiO_2 coatings deposited by the electrophoretic deposition process. *Proc. Inst. Mech. Eng. C J. Mech. Eng. Sci.* **2020**, *234*, 1231–1238. [CrossRef]
23. Gassoumi, B.; Jaballah, R.; Boukhachem, A.; Kamoun-Turki, N.; Amlouk, M. Simple route deposition and some physical investigations on nanoflower $NiMoO_4$ sprayed thin films. *Bull. Mater. Sci.* **2021**, *44*, 128. [CrossRef]
24. Larbi, T.; Ouni, B.; Boukachem, A.; Boubaker, K.; Amlouk, M. Electrical measurements of dielectric properties of molybdenum-doped zinc oxide thin films. *Mater. Sci. Semicond. Process.* **2014**, *22*, 50–58. [CrossRef]
25. Mrabet, C.; Boukhachem, A.; Amlouk, M.; Manoubi, T. Improvement of the optoelectronic properties of tin oxide transparent conductive thin films through lanthanum doping. *J. Alloys Compd.* **2016**, *666*, 392–405. [CrossRef]
26. Oliver, W.C.; Pharr, G.M. An improved technique for determining hardness and elastic modulus using load and displacement sensing indentation experiments. *J. Mater. Res.* **1992**, *7*, 1564–1583. [CrossRef]
27. Anurag, K.P.; Gautam, R.K.; Behera, C.K. Corrosion and wear behavior of Ti–5Cu-xNb biomedical alloy in simulated body fluid for dental implant applications. *J. Mech. Behav. Biomed. Mater.* **2023**, *137*, 105533.
28. Nathanael, A.J.; Mangalaraj, D.; Ponpandian, N. Controlled growth and investigations on the morphology and mechanical properties of hydroxyapatite/titania nanocomposite thin films. *Compos. Sci. Technol.* **2010**, *70*, 1645–1651. [CrossRef]
29. Singh, B.; Singh, G.; Sidhu, B.S. Investigation of the in vitro corrosion behavior and biocompatibility of niobium (Nb)-reinforced hydroxyapatite (HA) coating on CoCr alloy for medical implants. *J. Mater. Res.* **2019**, *34*, 1678–1691. [CrossRef]
30. Lee, S.W.; Paraguay-Delgado, F.; Arizabalo, R.D.; Gómez, R.; Rodríguez-González, V. Understanding the photophysical and surface properties of TiO_2–Al_2O_3 nanocomposites. *Mater. Lett.* **2013**, *107*, 10–13. [CrossRef]
31. Singh, G.; Singh, S.; Prakash, S. Surface characterization of plasma sprayed pure and reinforced hydroxyapatite coating on Ti6Al4V alloy. *Surf. Coat. Technol.* **2011**, *205*, 4814–4820. [CrossRef]
32. So, W.W.; Park, S.B.; Kim, K.J.; Moon, S.J. Phase transformation behavior at low temperature in hydrothermal treatment of stable and unstable titania. *Sol. J. Colloid. Interf. Sci.* **1997**, *191*, 398–406. [CrossRef] [PubMed]
33. Sujaridworakun, P.; Koh, F.; Fujiwara, T.; Pongkao, D.; Ahniyaz, A.; Yoshimura, M. Preparation of anatase nanocrystals deposited on hydroxyapatite by hydrothermal treatment. *Mater. Sci. Eng. C* **2005**, *25*, 87–91. [CrossRef]
34. Nathanael, A.J.; Mangalaraj, D.; Chen, P.C.; Ponpandian, N. Mechanical and photocatalytic properties of hydroxyapatite/titania nanocomposites prepared by combined high gravity and hydrothermal process. *Compo. Sci. Technol.* **2010**, *70*, 419–426. [CrossRef]
35. Dhiflaoui, H.; Ben Jaber, N.; Simescu Lazar, F.; Faure, J.; Ben Cheikh Larbi, A.; Benhayoune, H. Effect of annealing temperature on the structural and mechanical properties of coatings prepared by electrophoretic deposition of TiO_2 nanoparticles. *Thin Solid Film.* **2017**, *638*, 201–212. [CrossRef]
36. Rouchdi, M.; Salmani, E.; Fares, B.; Hassanain, N.; Mzerd, A. Synthesis and characteristics of Mg doped ZnO thin films: Experimental and abinitio study. *Results Phys.* **2017**, *7*, 620–627. [CrossRef]
37. Lee, S.H.; Kim, H.E.; Kim, H.W. Nano-sized hydroxyapatite coatings on Ti substrate by E beam deposition. *J. Am. Ceram. Soc.* **2007**, *90*, 50–56. [CrossRef]
38. Fathi, M.H.; Azam, F. Novel hydroxyapatite/tantalum surface coating for metallic dental implant. *Mater. Lett.* **2007**, *61*, 1238–1241. [CrossRef]
39. Amaravathy, P.; Sathyanarayanan, S.; Sowndarya, S.; Rajendran, N. Bioactive HA/TiO_2 coating on magnesium alloy for biomedical applications. *Ceram. Int.* **2014**, *40*, 6617–6630. [CrossRef]
40. Moskalewicz, T.; Łukaszczyk, A.; Kruk, A.; Kot, M.; Jugowiec, D.; Dubiel, B.; Radziszewska, A. Porous HA and nanocomposite nc-TiO_2/HA coatings to improve the electrochemical corrosion resistance of the Co-28Cr-5Mo alloy. *Mater. Chem. Phys.* **2017**, *199*, 144–158. [CrossRef]
41. Dhiflaoui, H.; Dabaki, Y.; Zayani, W.; Debbich, H.; Faure, J.; Ben Cheikh Larbi, A.; Benhayoune, H. Effects of Hydrogen Peroxide Concentration and Heat Treatment on the Mechanical Characteristics and Corrosion. *J. Mater. Eng. Perform.* **2023**, *in press*. [CrossRef]
42. Ahmadi, R.; Afshar, A. In vitro study: Bond strength, electrochemical and biocompatibility; evaluations of TiO_2/Al_2O_3 reinforced hydroxyapatite sol–gel coatings on 316L SS. *Surf. Coat. Technol.* **2021**, *405*, 126594. [CrossRef]
43. Zayani, W.; Azizi, S.; El-Nasser, K.S.; Othman Ali, I.; Molière, M.; Fenineche, N.; Mathlouthi, H.; Lamloumi, J. Electrochemical behavior of a spinel zinc ferrite alloy obtained by a simple sol-gel route for Ni-MH battery applications. *Int. J. Energy Res.* **2020**, *45*, 5235–5247. [CrossRef]